Noncollinear twisted RKKY interaction on the optically driven SnTe(001) surface

Mohsen Yarmohammadi [1,*] Marin Bukov [2,3,†] and Michael H. Kolodrubetz [1,‡]

[1]*Department of Physics, The University of Texas at Dallas, Richardson, Texas 75080, USA*

[2]*Max Planck Institute for the Physics of Complex Systems, Nöthnitzer Strasse 38, 01187 Dresden, Germany*

[3]*Faculty of Physics, Saint Kliment Ohridski University of Sofia, 5 James Bourchier Boulevard, 1164 Sofia, Bulgaria*

The nontrivial spin texture on the (001) surface of topological crystalline insulator SnTe hosts exotic scientific importance and spintronic applications. Here, we study the effects of weak Floquet optical driving on the Ruderman-Kittel-Kasuya-Yosida (RKKY) interaction between two magnetic impurities on a doped SnTe(001) surface. Due to peculiar spin-orbit hybridization, we find a noncollinear twisted RKKY interaction with XYZ-Heisenberg, symmetric in-plane, and asymmetric Dzyaloshinskii-Moriya (DM) terms. We see that contributions from the z (x) component of the XYZ-Heisenberg (DM) interaction are dominant for most parameters. The interactions, including DM terms that are responsible for interesting spin textures, require doping in most cases. We propose to modify the interactions *in situ* via optical control of band structure, and thereby doping. A notable aspect of this control protocol is breaking of electron-hole symmetry, which stems from the DM interaction.

I. INTRODUCTION

For the past decade, topological insulators (TIs) have been at the forefront of condensed matter physics [1,2]. Due to the strong spin-orbit coupling (SOC) [3,4], topological phases of matter contain gapped bulk and gapless surface states, protected by the time-reversal symmetry. Notably, quantum anomalous Hall effect (QAHE) has been observed in magnetically doped TIs [5–8], which is a topological effect with potential for low-power information processing associated with dissipationless chiral edge transport [9]. However, the QAHE becomes weak in a wide variety of transition metal-doped TIs [7,10–13] if one increases the density of surface carriers, mainly due to weakening of the magnetic order as a prerequisite for anomalous Hall physics.

Although the mechanism of this phenomenon is still under discussion [14,15], it was suggested that the indirect Ruderman-Kittel-Kasuya-Yosida (RKKY) exchange coupling between magnetic ions/impurities plays a significant role [16,17] among other common types of magnetism because it is tightly connected to the density of itinerant electrons in the host material [18]. Depending on the spin-orbit structures of topological materials, various types of RKKY mechanisms [19–21] and eventually different weak/strong regimes of QAHE can emerge. Furthermore, emergent spintronic applications need the RKKY mechanism to find the proper material with improved adjustability of spin alignments for logic magnetic devices [22,23]. It is the latter purpose that we mainly aim at in this paper, and we only conceptually (i.e., without additional calculations) state its relationship with the QAHE.

It has been shown that nontrivial RKKY interactions can appear on the surface of three-dimensional TIs [17,24–26] as well as at the edge of two-dimensional TIs [27–29]. In the work by Zyuzin and Loss [30], a long-range in-plane antiferromagnetic RKKY interaction has been found via a gap induced by placing a superconductor on the top of a TI. In the work by Lopes *et al.* [31], magnetic interactions between transition metal ions in a bismuthene TI with protected edge states showed that the direct overlap between the transition metal prevails in gapped bulk bismuthene. At the same time, a long-range magnetism is present at the borders of nanoribbons. Moreover, it has been reported that the RKKY interaction consisting of Heisenberg, Dzyaloshinskii-Moriya (DM), in-plane, and out-of-plane Ising terms can be formed on the edge of a two-dimensional TI when time-reversal symmetry is weakly broken [32].

In this paper, we proceed with the topological crystalline insulators (TCIs) [33–37] because, in addition to the time-reversal symmetry, crystal symmetries protect gapless surface states as well. This, in turn, covers a broad range of materials rather than specific TI compounds. Moreover, in contrast to an odd number of Dirac cones in strong TIs, TCIs provide an even number of cones, useful for spintronics and valleytronics [22,23,38]. We choose to focus on the SnTe(001) surface as one of the well-known TCIs with a *nontrivial spin texture* [39] to see how its magnetic features can go beyond the ones in TIs to be reflected in spintronics and QAHE physics.

In order to understand novel features in these materials, we need the ability to tune the properties of the surface. The best way to do so is through a gap opening at Dirac cones because it suppresses the large density of the doped surface around the Fermi energy, first, and second, it makes the magnetic order strong enough through the suppression of various phase alterations of ferromagnetic (FM) and antiferromagnetic (AFM) interactions. Among various ways for gap opening [40], we proceed with optical driving using

*mohsen.yarmohammadi@utdallas.edu
†mgbukov@phys.uni-sofia.bg
‡mkolodru@utdallas.edu

Floquet-Bloch states [41–44] because by tuning the intensity and frequency of the radiation, one can dynamically tune the photon-dressed bands, and eventually modulate the properties of an irradiated system in a controlled way. In the work by Asmar and Tse [45], it has been reported that the RKKY interaction mediated by a two-dimensional electron system subjected to a weak periodic driving shows oscillations with a period tunable by the light amplitude and frequency. Very recently, a study of the impurity states and RKKY interaction in irradiated graphene [46] has shown that under irradiation, a dynamical band gap opens up at the Dirac point in graphene, allowing impurity levels to exist inside the gap.

Motivated by various light-induced phenomena [47–52], we consider the interaction of a weak (to avoid the heating issue) circularly polarized light with the SnTe(001) surface, which opens a gap isotropically at all four Dirac cones, and thereby modulates the RKKY interaction. Subsequently, assuming that particles fill the Floquet-Bloch bands up to a given chemical potential when the weak Floquet drive is turned on, we pose the following question: how does the interplay between doping and optical driving influence the RKKY interaction for both spintronics and QAHE treatment? To answer this question, we reformulate the Heisenberg RKKY interaction [53,54] of hybrid states of sublattices in SnTe(001) for the bare spin-orbital states of each sublattice to take into account the effect of a nontrivial spin texture. This results in *noncollinear twisted spin alignments* including XYZ-Heisenberg, symmetric in-plane, and asymmetric DM interactions, implying that magnetic moments lie on the surface with increased adjustability. The asymmetric DM interaction is substantial for spintronic applications [55–57]. Interestingly, the Floquet drive tends to treat the QAHE by suppressing the density of doped states and RKKY amplitudes; however, we note that topological features of the SnTe(001) surface are not essential for our paper.

This paper is structured as follows. In Sec. II, we present the continuum Hamiltonian of a pristine SnTe(001) surface and construct the main building block of optically driven states. In Sec. III, we turn to the RKKY theory and derive the Floquet-Green's functions for a weak and off-resonant drive. The numerical results are presented in Sec. IV. We discuss potential extensions in Sec. V and finally we end the paper with a conclusion in Sec. VI.

II. HAMILTONIAN MODEL

A. Pristine SnTe(001)

In this section, we introduce the continuum Hamiltonian model [34–37,40,58] to describe each coaxial Dirac cone in the low-energy limit of the SnTe(001) surface. Two cones Λ_x and Λ'_x are located along the direction X_1-Γ-X_1 of the projected surface Brillouin zone (SBZ), while two cones Λ_y and Λ'_y are located along the direction X_2-Γ-X_2, as shown in the left side of Fig. 1. The pristine Hamiltonian of the Λ_x point is given by ($\hbar = 1$) [40,53,54,58–60]

$$\mathcal{H}_{\Lambda_x} = \tilde{\eta}_x p_x \sigma_y - \tilde{\eta}_y p_y \sigma_x, \tag{1}$$

where $p_x = k_x - |\vec{\Lambda}_x|$ is measured from the Dirac cone at $\vec{\Lambda}_x = (\sqrt{n^2 + \delta^2}/\eta_x, 0)$, $p_y = k_y$, $\tilde{\eta}_x = (\delta/\sqrt{n^2 + \delta^2})\eta_x$, and $\tilde{\eta}_y = \eta_y$ [59]. Here, $\eta_x = 3.53$ eV Å and $\eta_y = 1.91$ eV Å re-
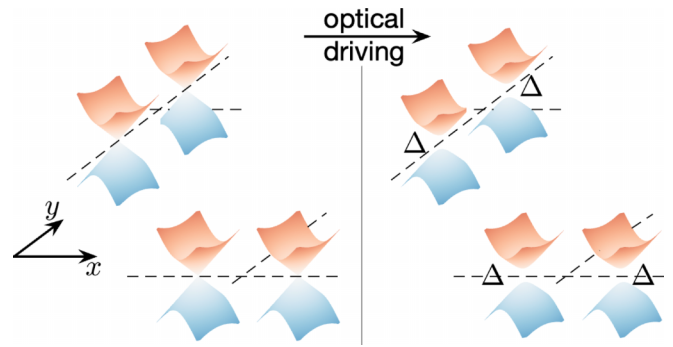

FIG. 1. The low-energy spectrum of Dirac fermions on the SBZ of the SnTe(001) surface, left side, and the optically driven spectrum, right side, with induced gap $\Delta = 2a^2/\Omega$ from the light with the ac field a and the frequency Ω. Other Dirac cones follow from C_2 and C_4 rotational symmetries.

fer to the bare Fermi velocities along the x and y direction, respectively. The Pauli matrices are given by σ_x and σ_y and act on sublattice spaces. The intervalley scattering parameters $n = 55$ meV and $\delta = 40$ meV are, respectively, responsible for the high-energy Dirac cones and the formation of two copies of Dirac cones with opposite chiralities in the four-band model (not shown here) [34,40,53,58]. Although they correctly describe intervalley scattering at the lattice scale of SnTe(001), they vary sample to sample since they arise from nonuniversal effects such as surface roughness. Indeed, the parameter n is the threshold energy below which the low-energy model is valid.

The rotational symmetry C_2 protects the coaxial Dirac cones resulting in $\mathcal{H}_{\Lambda'_{x,y}} = \mathcal{H}_{\Lambda_{x,y}}$, while the perpendicular cones are formed by the C_4 symmetry. This, in turn, implies that $\mathcal{H}_{\Lambda_y} = \tilde{\eta}_y p_x \sigma_y - \tilde{\eta}_x p_y \sigma_x$. It should be stressed that the valence and conduction bands of the energy spectrum refer to the hybridized p orbitals of the cation Sn^{2+} and anion Te^{2-} sublattices, namely, $|1\rangle = (|\uparrow, Te\rangle + |\downarrow, Sn\rangle)/\sqrt{2}$ and $|2\rangle = (|\uparrow, Sn\rangle + |\downarrow, Te\rangle)/\sqrt{2}$ [39,40,58,59].

Before turning to the irradiated SnTe(001) surface, we make one useful simplification, which will help later to find analytical RKKY interactions. The anisotropy of the Fermi velocity along x and y directions can affect the band structure [61]. However, to include each Dirac cone separately in the RKKY interaction, we work with small momentum and by this we neglect the anisotropy feature of the surface Dirac cones originating from $\tilde{\eta}_x \simeq 2.08$ eV Å and $\tilde{\eta}_y = 1.91$ eV Å. Hence, we set $v_F = (\tilde{\eta}_x + \tilde{\eta}_y)/2 \simeq 2$ eV Å.

B. Irradiated SnTe(001)

In this section, we present the expression for the effective two-band Hamiltonian model discussed above for the case when the SnTe(001) Dirac cones are *weakly* driven by a circularly polarized light. To do so, the time-periodic vector potential $\vec{A}(t) = A_0[\sin(\Omega t), \cos(\Omega t)]$, where $A_0 = E_0/\sqrt{2}\Omega$ (E_0 and Ω are the amplitude and frequency of light, respectively) is chosen to drive the Hamiltonian of the Λ_x point (and

other Dirac cones) through the minimal coupling scheme as

$$\mathcal{H}_{\Lambda_x}(t) = \begin{pmatrix} 0 & -iv_F p_- - ae^{+i\Omega t} \\ +iv_F p_+ - ae^{-i\Omega t} & 0 \end{pmatrix}, \quad (2)$$

where $p_\pm = p_x \pm ip_y$ and $a = eA_0v_F$. The drive induces transitions between the eigenstates. Since the Hamiltonian is periodic in time, $\mathcal{H}_{\Lambda_x}(t) = \mathcal{H}_{\Lambda_x}(t + T)$ with $T = 2\pi/\Omega$, the valid theory to address the time-periodic Hamiltonians is the Floquet-Bloch theorem [44,62]: a complete set of solutions of the time-dependent Schrödinger equation $\mathcal{H}_{\Lambda_x}(t)|\psi(t)\rangle = i\partial_t|\psi(t)\rangle$ reads as $|\psi_{f,p}(t)\rangle = e^{-i\varepsilon_{f,p}}|\mathcal{F}_{f,p}(t)\rangle$, where the integer Floquet index f classifies different sidebands with energies $\varepsilon_{f,p}$. Accordingly, the Fourier series $|\mathcal{F}_{f,p}(t)\rangle = \sum_{j=-\infty}^{\infty} e^{-ij\Omega t}|\mathcal{F}_{f,p}^j\rangle$ describes the time-periodic Floquet states $|\mathcal{F}_{f,p}(t)\rangle = |\mathcal{F}_{f,p}(t + 2\pi/\Omega)\rangle$. It should be mentioned that $f = 0$ maps the quasienergies to the first Floquet zone $[-\Omega/2, \Omega/2]$. Then, it is straightforward to deduce the Floquet Hamiltonian $\mathcal{H}_{F,\Lambda_x} = \mathcal{H}_{\Lambda_x}(t) - i\partial_t$ in the Fourier domain [63] $\sum_{j=-\infty}^{\infty} \mathcal{H}_{F,mj}|\mathcal{F}_{f,p}^j\rangle = \varepsilon_{f,p}|\mathcal{F}_{f,p}^m\rangle$. Having the driving period $T = 2\pi/\Omega$, the matrix elements of the Floquet Hamiltonian can be found via $\mathcal{H}_{F,mj} = \mathcal{H}_{mj} - j\Omega\delta_{m,j}$, where j is the photon number and [64–66]

$$\mathcal{H}_{mj} = \frac{1}{T} \int_0^T \mathcal{H}_{\Lambda_x}(t) e^{i(m-j)\Omega t} dt. \quad (3)$$

The Floquet Hamiltonian can be numerically diagonalized to study the exact dynamics governed by the application of light. However, for sufficiently weak electric field intensities, i.e., when the field intensity a is small compared to the frequency Ω, we may approximate the Floquet Hamiltonian using a high-frequency expansion explained below. In the high-frequency limit, the Floquet sidebands do not overlap; thus, there are no gaps due to band crossings so the hybridization between different Floquet bands becomes weak, meaning that interband transitions of electrons are suppressed.

Thus, using a perturbative approach known as the Van Vleck inverse-frequency expansion, we obtain the effective Floquet Hamiltonian in powers of Ω^{-1}, $\mathcal{H}_{F,\Lambda_x} \simeq \mathcal{H}_{\Lambda_x} + \frac{[\mathcal{H}_{-1}, \mathcal{H}_{+1}]}{\Omega}$ [43,43,67,68], which reads as

$$\mathcal{H}_{F,\Lambda_x} = \begin{pmatrix} +\Delta/2 & -iv_F p e^{-i\varphi_p} \\ +iv_F p e^{+i\varphi_p} & -\Delta/2 \end{pmatrix}, \quad (4)$$

where $\varphi_p = \tan^{-1}(p_y/p_x)$ and a gap $\Delta = 2a^2/\Omega$ opens up at the Dirac cone through a two-photon process similar to that in Refs. [41,64,66,69,70]. Using the C_2 and C_4 symmetries, one can obtain the Floquet Hamiltonian at other Dirac cones. Diagonalizing the above Hamiltonian leads to a gapped Dirac dispersion $\mathcal{E}_{\Lambda_x}(p) = \pm\sqrt{v_F^2 p^2 + \Delta^2/4}$, as shown in the right panel of Fig. 1.

In addition to optical driving, there are various ways to open the gap at the Dirac cones [40], namely, the exchange magnetization, the Zeeman term without an external magnetic field, and proximity coupling to a ferromagnet. However, despite restrictions in applying other sources of gap opening (e.g., a proper direction is essential for the exchange field induced by proximity coupling to a ferromagnet), the Floquet drive allows us to tune the properties of the dispersion for various purposes by adjusting the intensity and frequency of
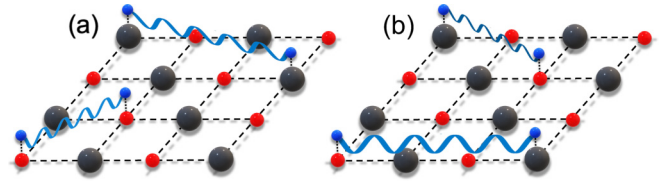

FIG. 2. A simple schematic for the position of magnetic impurities on (a) the same and (b) different sublattices of the SnTe(001) surface. Cation Sn^{2+}, anion Te^{2-}, and the local magnetic impurities are, respectively, shown by the black, red, and blue spheres.

light. Moreover, further photon processes in $\mathcal{H}_{F,\Lambda_x}$ can be taken into account by including higher-order terms [64,64,66].

For our purposes, the Floquet drive will be used to tune the RKKY interaction for both spintronics and eventually QAHE physics (indirectly through the density of surface carriers). We now proceed to the RKKY interaction in irradiated SnTe(001).

III. RKKY INTERACTION IN IRRADIATED SnTe(001)

As explained in the introduction, the indirect exchange coupling between two magnetic impurities or two localized spins $\vec{S}_1$ and $\vec{S}_2$ mediated by the host itinerant electron spins $\vec{s}$ is described by RKKY theory [18]. In our case, the host itinerant electrons are the optically driven ones on the SnTe(001) surface given by Eq. (4). According to this theory, the magnetic moments are treated as immobile defects on the lattice sites $\vec{R}_1$ and $\vec{R}_2$, and the interaction Hamiltonian is given by $\mathcal{H}_{int} = J \sum_i \vec{S}_i \cdot \vec{s}_i$, where J denotes the bare exchange energy. Thus, we consider the total Hamiltonian for the SnTe(001) surface including a contact interaction with the magnetic centers, namely, $\mathcal{H} = \mathcal{H}_{F,\Lambda_x} + \mathcal{H}_{int}$. Using second-order perturbation theory, one finds [18]

$$\mathcal{H}_{RKKY}^{\alpha\beta} = J^2 \sum_{l,j} S_1^{l\alpha} \chi_{lj}^{\alpha\beta}(\vec{R}) S_2^{j\beta}, \quad (5)$$

with lattice sites α and β, and the impurity separation $\vec{R} = \vec{R}_2 - \vec{R}_1$. In the above equation, the spin susceptibility $\chi_{lj}^{\alpha\beta}(\vec{R})$ can be obtained from the retarded Green's functions in the spin space for different flavors $\{l, j\} \in \{x, y, z\}$ [71–73]:

$$\chi_{lj}^{\alpha\beta}(\vec{R}) = -\frac{2}{\pi} \text{Im} \int_{-\infty}^{\mathcal{E}_F} d\mathcal{E} \, \mathbb{F}_{lj}^{\alpha\beta}(\mathcal{E}, \vec{R}), \quad (6)$$

where $\mathcal{E}_F$ is the Fermi energy and

$$\mathbb{F}_{lj}^{\alpha\beta}(\mathcal{E}, \vec{R}) = \text{Tr}[\sigma_l G^{\alpha\beta}(\mathcal{E}, \vec{R})\sigma_j G^{\beta\alpha}(\mathcal{E}, -\vec{R})]. \quad (7)$$

The magnetic impurities can reside on the same, Fig. 2(a), or different, Fig. 2(b), sublattices. Other configurations, such as impurities on the bonds or in the center of the unit cell, can be simply obtained by adding together the results for the RKKY interaction on the nearby sites. For example, if one magnetic impurity is located halfway between a Sn site at location $a_0\hat{y}/2$ and Te site at $-a_0\hat{y}/2$ (a_0 is the lattice constant), then the interaction with an impurity located at a distance $\vec{R}$ away on a Sn site is given by $\mathcal{H}_{RKKY}^{bond} = \mathcal{H}_{RKKY}^{SnSn}(\vec{R} - a_0\hat{y}/2) + \mathcal{H}_{RKKY}^{TeSn}(\vec{R} + a_0\hat{y}/2)$. Note that the microscopic coupling J for this case will be different from the site-located impurity, and

will depend on the sublattice. Generalizations to other impurity positions are straightforward.

We set the temperature to zero in the present paper, so $\mathcal{E}_F = \mu$, where μ is the chemical potential. The role of doping is then characterized by $\mu > 0$ and $\mu < 0$ referring to electron and hole doping, respectively. We assume that the electrons fill all energies up to μ within the Floquet-modified dispersion because the optical drive considered is sufficiently weak and off resonant that it may be turned on continuously, resulting in a new (quasi-zero-temperature) steady state. Note that this is fundamentally different from many other Floquet systems which are experimentally constrained to pump-probe nonequilibrium states to avoid heating, for which the electron filling is quite different [74]. In Eq. (7), we have

$$
G^{\alpha\beta}(\mathcal{E}, \vec{R}) = \begin{pmatrix} G_{\alpha\beta}^{\uparrow\uparrow}(\mathcal{E}, \vec{R}) & G_{\alpha\beta}^{\uparrow\downarrow}(\mathcal{E}, \vec{R}) \\ G_{\alpha\beta}^{\downarrow\uparrow}(\mathcal{E}, \vec{R}) & G_{\alpha\beta}^{\downarrow\downarrow}(\mathcal{E}, \vec{R}) \end{pmatrix}, \quad (8)
$$

which denotes the real-space noninteracting Green's function of sublattices in spin space, given by the photodressed Dirac bands. However, we must sum over the directions X_1-Γ-X_1 and X_2-Γ-X_2 on the SnTe(001) surface, as well as the pair of Dirac cones at X_1 and X_2 points, to cover the entire SBZ. Thus, we have

$$
G_{\alpha\beta}^{\sigma\sigma'}(\mathcal{E}, \vec{R}) = \frac{1}{S_{\text{SBZ}}} \int d^2p \, e^{i\vec{p}\cdot\vec{R}} [e^{i\vec{X}_1 \cdot \vec{R}} G_{\alpha\beta}^{\sigma\sigma'}(\vec{p} + \vec{X}_1, \mathcal{E}) \\ + e^{i\vec{X}_2 \cdot \vec{R}} G_{\alpha\beta}^{\sigma\sigma'}(\vec{p} + \vec{X}_2, \mathcal{E})], \quad (9)
$$

with $\{\sigma, \sigma'\} = \{\uparrow, \downarrow\}$, where S_{SBZ} is the area of the entire SBZ. The integral is dominated by low momentum, $p \ll |\Lambda_{x,y}|$, justifying our choice to treat each Dirac cone independently in the low-energy limit of the two-band model. The momentum-space Green's functions in the above equation are given by $G(\vec{p} + \vec{X}_1, \mathcal{E}) = e^{i\Lambda_x R_x} \mathcal{G}^{\Lambda_x}(p, \mathcal{E}) + e^{-i\Lambda_x R_x} \mathcal{G}^{\Lambda'_x}(p, \mathcal{E})$ and $G(\vec{p} + \vec{X}_2, \mathcal{E}) = e^{i\Lambda_y R_y} \mathcal{G}^{\Lambda_y}(p, \mathcal{E}) + e^{-i\Lambda_y R_y} \mathcal{G}^{\Lambda'_y}(p, \mathcal{E})$, where $\mathcal{G}^{\Lambda'_{x/y}}(p, \mathcal{E}) = 1/\mathcal{E} + io^+ - \mathcal{H}_{F, \Lambda'_{x/y}}$.

It is necessary to point out that in the Hamiltonian model, a superposition of sublattices given by the eigenstates $|1\rangle$ and $|2\rangle$ appears, rather than the bare sublattices $|\text{Te/Se}, \uparrow / \downarrow\rangle$. Therefore, one needs to express the real-space Green's functions of the hybrid states in terms of the bare sublattices considering the corresponding spins. Hence, we rewrite the above Green's function as (see Appendix A)

$$
G_{\alpha\beta}^{\sigma\sigma'}(\mathcal{E}, \vec{R}) = \sum_{\gamma,\eta} u_{\alpha,\gamma,\sigma}^* u_{\beta,\gamma,\sigma'} \mathcal{G}_{\gamma\eta}(\mathcal{E}, \vec{R}), \quad (10)
$$

in which the summation runs over hybrid states $\{|1\rangle, |2\rangle\}$ and $u_{\text{Te},1,\uparrow} = u_{\text{Te},2,\downarrow} = u_{\text{Sn},1,\downarrow} = u_{\text{Sn},2,\uparrow} = 1/\sqrt{2}$. To calculate $\mathcal{G}_{\gamma\eta}(\mathcal{E}, \vec{R})$, we first calculate the reciprocal-space Green's functions around all Dirac cones within the weak-driven approximation. Therefore, using the relation $\mathcal{G}^{\Lambda_x}(p, \mathcal{E}) = [\mathcal{E} + io^+ - \mathcal{H}_{F,\Lambda_x}]^{-1}$ with infinitesimal parameter $o^+ \to 0$ for the Λ_x point as well as using the expressions $d^2p = p\,dp\,d\varphi_p$ and $\exp[i\vec{p}\cdot\vec{R}] = \exp[ipR\cos(\varphi_p - \varphi_R)]$ with $\varphi_p = \tan^{-1}(p_y/p_x)$, we obtain

$$
\mathcal{G}_{\gamma\eta}(\mathcal{E}, \vec{R}) = \frac{1}{S_{\text{SBZ}}} \int_0^{p_c} \int_0^{2\pi} d^2p\, e^{i\vec{p}\cdot\vec{R}} \mathcal{G}_{\gamma\eta}(p, \mathcal{E}). \quad (11)
$$

The details of the integration in the above equation are very similar to the ones reported in Refs. [71–73] and we would avoid repetition here. To obtain analytical expressions for a better understanding of numerical results, we set the cutoff $p_c \to \infty$. The validity of such an extension of the linearity of the Dirac bands to infinity has been well established in the above references such that both numerical short-range and long-range responses in the low-energy limit match the analytical results obtained from the above approximation. Although it is evident that for undoped states, the above extension perfectly works, the approximation maintains its validity in the presence of weak doping (to separate four Dirac cones) and driving (to avoid heating) potentials in our model. Hence, for the Λ_x point, the real-space Green's functions of hybrid states $|1\rangle$ and $|2\rangle$ read as

$$
\mathcal{G}_{11}(\mathcal{E}, \vec{R}) = \frac{-2\pi[\mathcal{E} + io^+ + \Delta/2]}{S_{\text{SBZ}}\, v_F^2} \mathbb{K}_0(-i\widetilde{\mathcal{E}} R/v_F), \quad (12a)
$$

$$
\mathcal{G}_{12}(\mathcal{E}, \vec{R}) = \frac{+2\pi\, i\, e^{-i\varphi_R}\widetilde{\mathcal{E}}}{S_{\text{SBZ}}\, v_F^2} \mathbb{K}_1(-i\widetilde{\mathcal{E}} R/v_F), \quad (12b)
$$

$$
\mathcal{G}_{21}(\mathcal{E}, \vec{R}) = \frac{-2\pi\, i\, e^{+i\varphi_R}\widetilde{\mathcal{E}}}{S_{\text{SBZ}}\, v_F^2} \mathbb{K}_1(-i\widetilde{\mathcal{E}} R/v_F), \quad (12c)
$$

$$
\mathcal{G}_{22}(\mathcal{E}, \vec{R}) = \frac{-2\pi[\mathcal{E} + io^+ - \Delta/2]}{S_{\text{SBZ}}\, v_F^2} \mathbb{K}_0(-i\widetilde{\mathcal{E}} R/v_F), \quad (12d)
$$

where $\widetilde{\mathcal{E}} = \sqrt{(\mathcal{E} + io^+)^2 - \Delta^2/4}$ and $\mathbb{K}_{0,1}$ denote modified Bessel functions. For the Λ'_x, Λ_y, and Λ'_y points, we have the exact same expressions since the gap is opened isotropically at all Dirac cones by the optical driving. The above elements fulfill the relations $\mathcal{G}_{11/22}(\mathcal{E}, -\vec{R}) = \mathcal{G}_{11/22}(\mathcal{E}, \vec{R})$ and $\mathcal{G}_{12/21}(\mathcal{E}, -\vec{R}) = -\mathcal{G}_{12/21}(\mathcal{E}, \vec{R})$.

Turning back to Eq. (5), one would rewrite the RKKY Hamiltonian as

$$
\mathcal{H}_{\text{RKKY}} = -\frac{2J^2}{\pi} \text{Im} \int_{-\infty}^{\mu} d\mathcal{E} \sum_{lj} S_1^l S_2^j \, \mathbb{F}_{lj}. \quad (13)
$$

The components $\mathbb{F}_{lj}^{\alpha\alpha}$ and $\mathbb{F}_{lj}^{\alpha\beta}$ for the spins on the same and different sublattices, respectively, are presented in Appendix B. Accordingly, the Hamiltonians read as

$$
\mathcal{H}_{\text{RKKY}}^{\alpha\alpha,\alpha_s} = \sum_i \mathcal{J}_i^{\alpha\alpha} S_1^i S_2^i + \vec{\mathcal{J}}_{\text{DM}}^{\alpha_s} \cdot (\vec{S}_1 \times \vec{S}_2)
$$
$$
+ \alpha_s \mathcal{J}_{xy}^{\alpha\alpha} [S_1^x S_2^y + S_1^y S_2^x], \quad (14a)
$$

$$
\mathcal{H}_{\text{RKKY}}^{\alpha\beta,\alpha_d} = \sum_i \mathcal{J}_i^{\alpha\beta} S_1^i S_2^i + \vec{\mathcal{J}}_{\text{DM}}^{\alpha_d} \cdot (\vec{S}_1 \times \vec{S}_2), \quad (14b)
$$

where we have $\vec{\mathcal{J}}_{\text{DM}}^{\alpha_s} = (\mathcal{J}_{\text{DM},x}^{\alpha\alpha}, \alpha_s \mathcal{J}_{\text{DM},y}^{\alpha\alpha}, 0)$, and $\vec{\mathcal{J}}_{\text{DM}}^{\alpha_d} = (\mathcal{J}_{\text{DM},x}^{\alpha\beta}, 0, \alpha_d \mathcal{J}_{\text{DM},z}^{\alpha\beta})$. When the impurities are placed on the TeTe (SnSn) sublattices, we use $\alpha_s = +1 (-1)$, while $\alpha_d = +1 (-1)$ for the TeSn (SnTe) sublattices. In general, for the sublattice setup, we continue only with $\alpha_s = +1$ in Eq. (14) henceforth for the magnetic impurities on the same TeTe sublattices. A sign change in $\widetilde{\mathcal{J}}_{\text{DM},y}^{\alpha\alpha}$ and $\widetilde{\mathcal{J}}_{xy}^{\alpha\alpha}$ gives rise to the results for magnetic impurities on the same SnSn sublattices; for different TeSn sublattices, one can simply use Eq. (17). Finally, the sign of $\widetilde{\mathcal{J}}_{\text{DM},z}^{\alpha\beta}$ should be swapped for the results on different SnTe sublattices.

The first terms in both Hamiltonians of Eq. (14) couple the same spin directions with different exchange strengths $\{\mathcal{J}_x, \mathcal{J}_y, \mathcal{J}_z\}$, which gives the XYZ-Heisenberg interaction. Furthermore, due to the intrinsic SOC of the SnTe(001) surface, the symmetry of spin space is expected to be broken in response to the impurities, leading to off-diagonal components of the RKKY Hamiltonian (the last terms) [75,76]. While the asymmetric second terms resemble a DM interaction, the third term in Eq. (14a) gives rise to an in-plane symmetric interaction. The large DM interaction (which we will show in the following) compared to the one in TI thin films [77] can lead to interesting phenomena such as spin Nernst effect, the appearance of the nontrivial topology, and topological spin excitations [78–80]. The DM interaction has been also explored extensively in recent years for spintronic applications [55–57,81]. These off-diagonal terms enable the full RKKY Hamiltonian to provide noncollinear twisted alignment between the magnetic impurities.

Let us define the form factor between Dirac points and $\{X_1$ and $X_2\}$ points from Eq. (9):

$$f(\vec{R}) = 2\left[e^{iX_1 R_x}\cos(\Lambda_x R_x) + e^{iX_2 R_y}\cos(\Lambda_y R_y)\right]. \quad (15)$$

For clarity, we work with the normalized exchange interactions, $\mathcal{C}\,J^2\,|f(\vec{R})|^2$, where $\mathcal{C} = 4\pi/S_{\mathrm{SBZ}}^2 v_{\mathrm{F}}^4$ and thus $\widetilde{\mathcal{J}}(R) = \mathcal{J}(R)/\mathcal{C}\,J^2\,|f(\vec{R})|^2$ suppresses the beating type of oscillations from the multiple surface Dirac cones [53], as shown in Fig. 6 of Appendix C. With this, we show the results for a single Dirac cone in what follows. The modulations captured in $|f(\vec{R})|^2$ are different than those of graphene and other systems [82–85] and can be useful to modulate the couplings on medium-length scales $1/\Lambda_{x,y}$. Crucially, such a length scale only exists in TCIs and is potentially tunable via, e.g., strain.

For numerical purposes, we first define $\mathcal{E} - \mu = \mathcal{E}'$, owing to the electron-hole symmetry [71–73,84], to set the upper limit of the integral in Eq. (13) to zero. Then, we use the imaginary energy representation $\mathcal{E}' + io^+ = i\omega$ to get rid of the numerical singularities and tight tolerances in the real energy integration. After simple algebra calculations and defining $\widetilde{\omega}^2 = (\omega - i\mu)^2 + (\Delta^2/4)$, the components of RKKY Hamiltonians for the first configuration (impurities on the same sublattices) read as

$$\widetilde{\mathcal{J}}_x^{\alpha\alpha}(R) = +\mathrm{Im}\int_{o^+}^{\infty}id\omega\,\widetilde{\omega}^2\big[\mathbb{K}_0^2(\widetilde{\omega}R/v_{\mathrm{F}})$$
$$+\cos(2\varphi_R)\mathbb{K}_1^2(\widetilde{\omega}R/v_{\mathrm{F}})\big], \quad (16a)$$

$$\widetilde{\mathcal{J}}_y^{\alpha\alpha}(R) = +\mathrm{Im}\int_{o^+}^{\infty}id\omega\,\widetilde{\omega}^2\big[\mathbb{K}_0^2(\widetilde{\omega}R/v_{\mathrm{F}})$$
$$-\cos(2\varphi_R)\mathbb{K}_1^2(\widetilde{\omega}R/v_{\mathrm{F}})\big], \quad (16b)$$

$$\widetilde{\mathcal{J}}_z^{\alpha\alpha}(R) = +\mathrm{Im}\int_{o^+}^{\infty}id\omega\,\widetilde{\omega}^2\big[\mathbb{K}_0^2(\widetilde{\omega}R/v_{\mathrm{F}}) + \mathbb{K}_1^2(\widetilde{\omega}R/v_{\mathrm{F}})\big]$$
$$-\frac{\Delta^2}{2}\mathrm{Im}\int_{o^+}^{\infty}id\omega\,\mathbb{K}_0^2(\widetilde{\omega}R/v_{\mathrm{F}}), \quad (16c)$$

$$\widetilde{\mathcal{J}}_{xy}^{\alpha\alpha}(R) = +\sin(2\varphi_R)\mathrm{Im}\int_{o^+}^{\infty}id\omega\,\widetilde{\omega}^2\,\mathbb{K}_1^2(\widetilde{\omega}R/v_{\mathrm{F}}), \quad (16d)$$

$$\widetilde{\mathcal{J}}_{\mathrm{DM},x}^{\alpha\alpha}(R) = -2\sin(\varphi_R)\,\mathrm{Im}\int_{o^+}^{\infty}d\omega\,\widetilde{\omega}\sqrt{\widetilde{\omega}^2 - \Delta^2/4}$$
$$\times\mathbb{K}_0(\widetilde{\omega}R/v_{\mathrm{F}})\,\mathbb{K}_1(\widetilde{\omega}R/v_{\mathrm{F}}), \quad (16e)$$

$$\widetilde{\mathcal{J}}_{\mathrm{DM},y}^{\alpha\alpha}(R) = -2\cos(\varphi_R)\,\mathrm{Im}\int_{o^+}^{\infty}d\omega\,\widetilde{\omega}\sqrt{\widetilde{\omega}^2 - \Delta^2/4}$$
$$\times\mathbb{K}_0(\widetilde{\omega}R/v_{\mathrm{F}})\,\mathbb{K}_1(\widetilde{\omega}R/v_{\mathrm{F}}). \quad (16f)$$

Due to the symmetrical form of the states $|1\rangle$ and $|2\rangle$, the x and y components of the XYZ-Heisenberg interaction differ only by a sign in the off-diagonal components of the real-space Green's functions. Moreover, the DM components are shifted by the $\pi/2$ phase.

For the second configuration (impurities on different sublattices), we find

$$\widetilde{\mathcal{J}}_x^{\alpha\beta}(R) = +\widetilde{\mathcal{J}}_x^{\alpha\alpha}(R), \quad (17a)$$

$$\widetilde{\mathcal{J}}_y^{\alpha\beta}(R) = -\widetilde{\mathcal{J}}_y^{\alpha\alpha}(R), \quad (17b)$$

$$\widetilde{\mathcal{J}}_z^{\alpha\beta}(R) = -\widetilde{\mathcal{J}}_z^{\alpha\alpha}(R), \quad (17c)$$

$$\widetilde{\mathcal{J}}_{\mathrm{DM},x}^{\alpha\beta}(R) = -\widetilde{\mathcal{J}}_{\mathrm{DM},x}^{\alpha\alpha}(R), \quad (17d)$$

$$\widetilde{\mathcal{J}}_{\mathrm{DM},z}^{\alpha\beta}(R) = -\widetilde{\mathcal{J}}_{xy}^{\alpha\alpha}(R), \quad (17e)$$

stemming from the spin-orbit structure of the model, and not from the spatial symmetry of the SnTe(001) surface.

IV. RESULTS AND DISCUSSION

The role of the chemical potential μ and the optical gap Δ in various terms of the RKKY interaction form the main messages of the present paper for both spintronic applications and QAHE physics. The Fermi sea can be drained out if one keeps increasing the driving strength for a fixed impurity separation R and direction φ_R. This, in turn, manipulates the surface states involved in the RKKY coupling. It is very important to control the chemical potential to bring the surface states into the so-called low-energy regime. This can be tuned with, e.g., a back gate from the thin film substrates [86,87].

It is necessary to mention that the Floquet parameter a/Ω mainly tunes the light-matter interaction effect on the SnTe(001) surface, which should be small in the weak drive regime (to avoid heating of the sample). It is worthwhile commenting that the alignment of magnetic moments can be influenced by both a and Ω. In Fig. 7 of Appendix D, we systematically address this matter. As soon as we turn on the light, independent of the symmetric and asymmetric contributions to the RKKY interaction, magnetic moments talk to each other only beneath the line $a \propto \sqrt{\Omega}$. The bandwidth of our model is given by $2n = 110$ meV. To have a broader range of light intensity for tuning the RKKY interaction (less zero response), we continue with an off-resonant high-frequency $\Omega = 1$ eV $\propto 270$ THz much larger than the bandwidth. Thus, the gap of the system can reach $\Delta \simeq 23$ K [88], i.e., $a \simeq 47$ meV. However, we vary intensity a up to 200 meV (optical gap Δ up to 80 meV) in what follows.

From Eqs. (16a)–(16f) and (17a)–(17e), one can observe the periodicity of interactions in φ_R—except φ_R-independent $\widetilde{\mathcal{J}}_z^{\alpha\alpha}(R)$—which provides $\mathcal{H}_{\mathrm{RKKY}}(\varphi_R) = \mathcal{H}_{\mathrm{RKKY}}(\varphi_R + \pi)$. Due to the square lattice of the host SnTe(001) surface, three angles $\varphi_R = 0$, $\pi/4$, and $\pi/2$ between the magnetic impurities lead to special RKKY interactions. A quick analysis results in $\widetilde{\mathcal{J}}_{xy}^{\alpha\alpha}(R) = 0$ for both 0 and $\pi/2$ and $\widetilde{\mathcal{J}}_{\mathrm{DM},x/y}^{\alpha\alpha}(R) = 0$, respectively, for 0 and $\pi/2$, while for $\pi/4$, we find
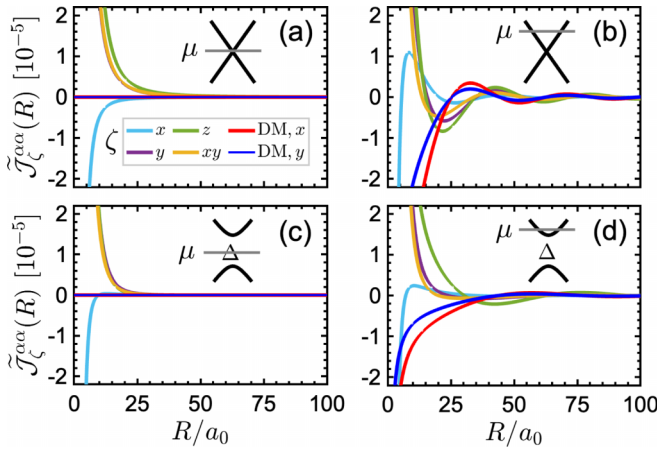
FIG. 3. RKKY interactions on the SnTe(001) surface at $\varphi_R = \pi/3$ as a function of impurity separation R when the surface is (a) pristine (undriven-undoped), (b) undriven-doped, (c) driven-undoped, and (d) driven-doped. We set $\mu = 27.5$ meV and $\Delta = 45$ meV, respectively, for the chemical potential and optical gap. It can be observed that the asymmetric DM term exists only on the doped surface. Furthermore, the Floquet drive suppresses all terms due to the reduced density of mediating states.

$\widetilde{\mathcal{J}}_x^{\alpha\alpha}(R) = \widetilde{\mathcal{J}}_y^{\alpha\alpha}(R)$ and $\widetilde{\mathcal{J}}_{\mathrm{DM},x}^{\alpha\alpha}(R) = \widetilde{\mathcal{J}}_{\mathrm{DM},y}^{\alpha\alpha}(R)$. But, for non-collinear twisted alignments of magnetic moments on the surface with more adjustability, we continue with an in-plane angle, e.g., $\varphi_R = \pi/3$. For other angles, sine and cosine prefactors in Eq. (16) will be changed, which do not affect the main messages of the present paper. We set the chemical potential and the optical gap at $\mu = 27.5$ meV and $\Delta = 45$ meV, respectively, where necessary. In the driven-doped surface, this set helps to have effective interactions because of $\mu > \Delta/2$ (see interpretation below).

Figure 3 shows the RKKY terms as a function of impurity separation R/a_0. For the pristine (undriven-undoped) surface, $\mu = 0$ and $\Delta = 0$, which leads to real $\widetilde{\omega} = \omega$, the analytical solution of Eqs. (16a)–(16d) is already known [53,54,71–73,85] and can straightforwardly be found with the help of Eq. (E1) in Appendix E such that the nonzero interactions decay as R^{-3} [see Fig. 3(a)]. Under the same conditions, the DM terms in Eqs. (16e) and (16f) vanish, $\widetilde{\mathcal{J}}_{\mathrm{DM},x/y}^{\alpha\alpha}(R) = 0$, due to the absence of imaginary energy. The physical reason for a vanishing DM interaction stems from the presence of inversion symmetry between sublattices (absence of μ) for which asymmetric alignment of spins from the interplay of diagonal and off-diagonal spin-orbital states does not take place. The presence of DM interaction due to doping has been experimentally confirmed in TI thin films [56]. Interestingly, only $\widetilde{\mathcal{J}}_x^{\alpha\alpha}(R)$ forms an AFM order since the responses from different spin-orbital states, $\{|1\rangle$ and $|2\rangle\}$ or $\{|2\rangle$ and $|1\rangle\}$, are three times larger than the same spin-orbital states, $\{|1\rangle$ and $|1\rangle\}$ or $\{|2\rangle$ and $|2\rangle\}$, resulting in $\widetilde{\mathcal{J}}_x^{\alpha\alpha}(R) < 0$. In fact, for FM characters of $\widetilde{\mathcal{J}}_y^{\alpha\alpha}(R)$ and $\widetilde{\mathcal{J}}_z^{\alpha\alpha}(R)$ in Fig. 3(a), one can use Eq. (E1), which makes Eq. (16b) positive because of $\cos(2\pi/3) = -1/2$. Also, Eq. (16c) at $\Delta = 0$ is positive for the same reason. For $\widetilde{\mathcal{J}}_x^{\alpha\alpha}(R)$, the second term of Eq. (16a) is larger than its first term and it becomes negative (AFM character). In the presence of Δ in Fig. 3(c), Eqs. (16a)–(16c)

remain positive. In the presence of μ in Figs. 3(b) and 3(d), negative signs in Eqs. (16e) and (16f) are the main reasons for DM terms.

For the undriven-doped surface, $\mu \neq 0$ and $\Delta = 0$, which leads to imaginary $\widetilde{\omega} = \omega - i\mu$, one needs Eq. (E2) in Appendix E. It is obvious that the short-range RKKY interactions are given by the power-law R^{-3}, while for the long-range couplings, oscillatory Meijer functions [89,90] emerge, as presented in Fig. 8. Our numerical data in Fig. 3(b) confirm this dependence. In contrast to the pristine surface, DM interactions wake up when the surface is doped for the same reason of inversion symmetry breaking between sublattices.

For the driven-undoped surface, $\mu = 0$ and $\Delta \neq 0$, which leads to real $\widetilde{\omega} = \sqrt{\omega^2 + \Delta^2/4}$, with the help of Eq. (E3) in Appendix E, we find short-range RKKY interactions $\propto R^{-3}$, while for the long-range interactions, one needs to use $\lim_{\Delta R/v_F \to \infty} \mathbb{K}_n(\Delta R/v_F) \simeq \sqrt{\pi v_F/2\Delta R} \exp(-\Delta R/v_F)$ and the Laplace method to obtain RKKY interactions $\propto (R/\Delta)^{-3/2} \exp(-2\Delta R/v_F)$ [71], which are again in agreement with the numerical results in Fig. 3(c). For the reason mentioned before about the doping effect on the DM interaction, one still expects a vanishing DM response for the driven-undoped surface.

For the driven-doped surface in Fig. 3(d), we consider the $\mu > \Delta/2$ regime where the chemical potential is outside the optical gap so the states added by doping play a role in RKKY interactions (for $\mu < \Delta/2$ the DM terms vanish). Although it is not easy to find analytical expressions for the driven-doped surface, we expect a modified version of Meijer functions for the long-range coupling as the interactions behave like the undriven-doped surface. However, we believe that the power-law R^{-3} is still valid for short-range couplings. As both driving and doping are present, the drastic change of oscillations for all RKKY components is evident. This is a direct consequence of the optical gap for which the corresponding density of mediating states in the RKKY interaction decreases, and thus, most of the doped states are washed out. For this reason, the oscillations are accompanied by smaller amplitudes compared to the undriven-doped surface. This is mainly where our contribution pays off in QAHE physics since magnetic characters focus more on purely positive (FM) and negative (AFM) signs.

It is also worth mentioning that various FM and AFM characters emerge for symmetric XYZ-Heisenberg $\widetilde{\mathcal{J}}_i$ and in-plane $\widetilde{\mathcal{J}}_{xy}$ components depending on the interplay between driving and doping, as well as between the impurity separation and direction. But, for the change of signs in DM components, one needs to take into account the chirality. When DM is positive, the coupling between magnetic impurities favors clockwise rotation, meaning that it tends to align right handedly more naturally than left. Similarly, a negative DM interaction favors counterclockwise rotation for magnetic moments.

To gain further insights into the gap dependency of interactions, we proceed to plot the RKKY couplings against the optical gap Δ for $\mu = 13.75$ meV, Fig. 4(a), and $\mu = 27.5$ meV, Fig. 4(b), at $R/a_0 = 50$ and $\varphi_R = \pi/3$. As soon as we turn on the Floquet drive, all interactions start to emerge due to the presence of μ. It is noteworthy that once the gap edge lies at the chemical potential level, i.e., when $\Delta = 2|\mu|$, they start to vanish because the doped states start to lie in
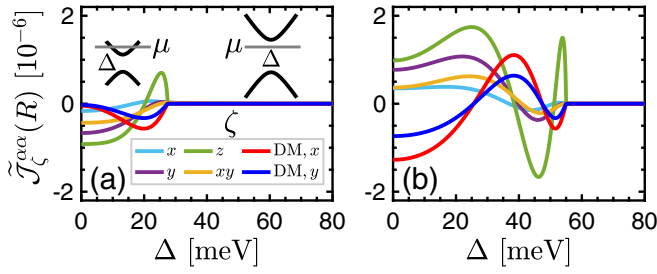
FIG. 4. RKKY interactions for (a) $\mu = 13.75$ meV and (b) $\mu = 27.5$ meV at $R/a_0 = 50$ and $\varphi_R = \pi/3$ as a function of the optical gap Δ on the SnTe(001) surface. Independent of the chemical potential, RKKY responses vanish for $\Delta \geqslant 2|\mu|$ once the chemical potential lies in the gap, due to their exponential decay with R.
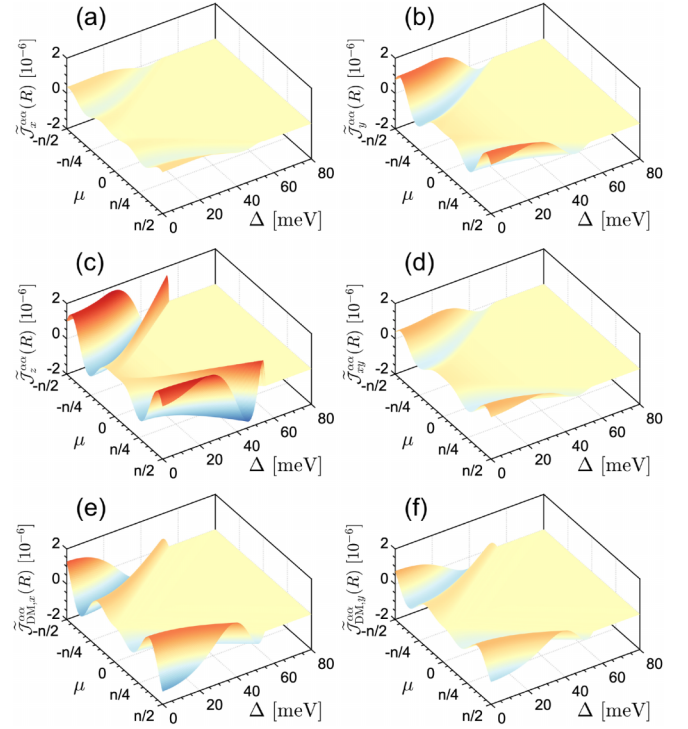

FIG. 5. RKKY interactions at $\varphi_R = \pi/3$ and $R/a_0 = 50$ as a function of both optical gap Δ and chemical potential μ on the driven-doped SnTe(001) surface. Red (blue) color refers to FM (AFM) order in (a)–(d), while they refer to clockwise (counterclockwise) spin rotation in the DM terms of (e) and (f). The yellow color depicts nearly zero RKKY response. The dominant contribution to the RKKY interaction belongs to the z (x) component of symmetric (asymmetric) interaction, i.e., $\widetilde{\mathcal{J}}_z^{\alpha\alpha}$ ($\widetilde{\mathcal{J}}_{\mathrm{DM},x}^{\alpha\alpha}$). As expected, no response appears for $\Delta \geqslant 2|\mu|$ due to the vanishing density of mediating states.

the gap without any significant density of mediating states. If we dope the surface stronger, Fig. 4(b), RKKY responses become stronger compared to Fig. 4(a). This can be easily understood by taking into account that the density of carriers on the surface with $\mu = 27.5$ meV is larger than at $\mu = 13.75$ meV; thus, more itinerant carriers act as mediators for the indirect exchange coupling between impurities.

Next, we systematically explore the RKKY interactions of the driven-doped SnTe(001) surface at fixed direction $\varphi_R = \pi/3$ and impurity separation $R/a_0 = 50$. In Fig. 5, at first glance, one would observe that the amplitude of oscillations increases as more surface states (larger μ) are involved in the exchange coupling. However, the gap opening reduces the rate of involved states and for a certain chemical potential μ, RKKY interactions are nonzero only below $\Delta = 2|\mu|$. For example, at $\mu = \pm 27.5$ meV, one obtains zero RKKY responses at $\Delta \geqslant 50$ meV, as confirmed in Figs. 5(a)–5(f), implying that there is no effective mediating state anymore on the surface (at least, within our approximations) so that the RKKY responses approach zero. The red and blue colors highlight the character of FM and AFM (clockwise and counter-clockwise spin rotations) for symmetric (asymmetric) RKKY components, while the yellow color displays nearly zero responses.

Additionally, the dominant oscillation amplitude belongs to the z component of the XYZ-Heisenberg, though the x component of the DM term is the next prevalent among others. As mentioned before, DM interaction enables the system to be applicable for emergent spintronic applications [55–57,81]. Although DM contribution is significant on the SnTe(001) surface, it also appears on the conventional surface of three-dimensional TIs [17,24–26] and at the edge of two-dimensional TIs [27–29], while it exceptionally vanishes in TI thin films [77]. Therefore, our large DM compatible with $\widetilde{\mathcal{J}}_z^{\alpha\alpha}(R)$ is a very useful feature of TCIs.

It is also worth exploring the intrinsic electron-hole symmetry on the driven-doped SnTe(001) surface. The electron-hole symmetry is valid for all symmetric interactions, XYZ-Heisenberg and in-plane xy, independent of doping and optical gap (also independent of the impurity separation and position of impurities—not shown here). For the DM interaction at a given direction, one immediately extracts the following relation:

$$\widetilde{\mathcal{J}}_{\mathrm{DM},x/y}^{\alpha\alpha}(-\mu, \Delta) = -\widetilde{\mathcal{J}}_{\mathrm{DM},x/y}^{\alpha\alpha}(+\mu, \Delta), \qquad (18)$$

which has already been confirmed experimentally on the surface of TI thin films [56], as also shown in Figs. 5(e) and 5(f). It has an opposite sign when the chemical potential cuts through the upper or lower band. We emphasize that the presence of inversion symmetry between sublattices and the corresponding spin-orbital states is the main origin of the above relationship.

For the experimental perspectives, one would extract the following critical Floquet driving amplitude E_0^c (considering an arbitrary driving frequency Ω) in the low-energy regime of the SnTe(001) surface above which a nearly zero RKKY coupling is achieved:

$$E_0^c = \frac{\sqrt{n}}{e v_{\mathrm{F}}} \Omega^{3/2}. \qquad (19)$$

For instance, in our case, for the selected light frequency of $\Omega \simeq 1$ eV, the Fermi velocity of $v_{\mathrm{F}} \simeq 2$ eV Å, and $n = 55$ meV, one finds $E_0^c \simeq 10^9$ V/m, which is nowadays easily realizable in experiment [91–93]. Having this information, we would suggest using a light intensity below E_0^c in experiments so tuning the RKKY coupling with light can play role in determining the prerequisites for spintronic applications and QAHE. Experimentally, single-atomic magnetometry and magnetotransport through scanning tunneling microscopy and

angle-resolved photoemission spectroscopy can measure the RKKY interaction [94–96].

V. OUTLOOK

Before closing the discussion, let us briefly discuss possible avenues for upcoming research. The present paper for the "weak" light-induced RKKY interaction, which still reports applicable findings, can also be addressed for the "strong" driving regime. First, in the strong driving regime, the full Floquet Hamiltonian is required for further photon processes [64]; second, the nonlinear corrections should be solved numerically [64,66]. The extended continuous strong driving must inevitably lead to heating, which without remediation would destroy the sample. We can propose a heat sink [97], which maintains a low system temperature despite the Floquet drive. Beyond the weak driving regime, our calculations could also be done for a "linearly" polarized light if one considers the nth-order Bessel functions for the corrections up to infinite orders [98].

To address the low-frequency limit beyond our high-frequency expansion, band crossings should also be considered in the theory; this requires another expansion of the effective Floquet Hamiltonian and extra terms will be generated. Additionally, the finite temperature effects can also be explored for both short- and long-range couplings within the finite-temperature self-consistent field approximation [99,100]. Stressing that the magnetic scattering potential may also happen between the magnetic impurities, the RKKY interaction can be approached beyond the linear response theory [101].

Note that the drive used to tune the RKKY interaction also opens up a topological gap in the surface Dirac cones. With four Dirac cones of identical chirality, it will correspond to Chern number 2, suggesting that TCIs may also be a useful playground for light-induced anomalous quantum Hall physics. Unlike existing two-dimensional systems, such as graphene [93], we propose to realize the gapped TCI surface states by continuous, moderate amplitude optical driving, which allowed the realization of an effective Fermi surface earlier in the paper, Sec IV. This also implies the quasistatic topology of the surface electronic states, which will be an interesting topic for future exploration. However, unlike graphene, this topological state is complicated by the presence of gapless edge states on the other [non-(001)] surfaces as well as the bottom (001) surface of the material. We leave an analysis of topological transport in this geometry for future work.

VI. CONCLUSIONS

Exploring the physics of magnetically doped topological systems in tuning QAHE as well as for the spintronics community has triggered interest in condensed matter physics. Recently, experimental photonic platforms have also become increasingly urgent for tuning the properties of materials. To contribute to these, we have employed the isotropic optically driven continuum model for Dirac cones with nontrivial spin textures on the doped SnTe(001) surface as a well-known TCI to investigate the (quasi)out-of-equilibrium physics of the

RKKY interaction between two magnetic impurities. This, in turn, aims at providing spintronic applications as well as making the TCI-based QAHE strong. To tune the features, in particular, we have focused on the weak driving effects and off-resonant regime between the light and bandwidth of the Dirac cones using the Van Vleck inverse-frequency expansion. We make use of the bare spin-orbital states of each sublattice, resulting in noncollinear twisted RKKY interaction with XYZ-Heisenberg, symmetric in-plane, and asymmetric DM terms.

Preliminary analyses highlighted the z (x) component of the XYZ-Heisenberg (DM) interaction as the first (second) dominant contribution to the total RKKY interaction. Moreover, depending on the position of magnetic impurities, chemical potential, and the optical gap, the driven-doped SnTe(001) surface reaches various modulations of FM and AFM characters for the symmetric RKKY terms as well as of the clockwise and counterclockwise spin rotations for the asymmetric DM ones. A systematic analysis of the RKKY coupling on the interplay between doping and driving demonstrated that the efficient range of chemical potential in controlling the amplitudes belongs to the strengths outside the optical gap. The optical gap (Floquet drive) in the presence of doping leads to a reduction of the RKKY amplitudes because of the decreased total density of mediating states. This is where we propose a Floquet drive to make the TCI-based QAHE strong when the surface is doped. Alongside, we find nonzero DM interactions only for the doped surface because of inversion symmetry breaking between sublattices. Moreover, to evaluate the intrinsic electron-hole symmetry of the system, we found that the symmetry is broken because of the DM term.

Providing reasonable light intensity and frequency compatible with the low-energy Dirac bands of the SnTe(001) surface, insights from the present paper are discussed for feasible experimental observations. Finally, we would mention that the large DM term on the surface of TCIs is highly desirable for spintronic applications, highlighting their additional usefulness compared to TIs due to the presence of multiple Dirac cones.

ACKNOWLEDGMENTS

APPENDIX A: COMPONENTS OF THE REAL-SPACE GREEN'S FUNCTION

The real-space Green's functions of hybrid states in terms of bare sublattices considering corresponding spins require the following definition $G_{\alpha\beta}^{\sigma\sigma'}(\mathcal{E}, \vec{R}) = \sum_{\gamma,\eta} u_{\alpha,\gamma,\sigma}^* u_{\beta,\gamma,\sigma'} \mathcal{G}_{\gamma\eta}(\mathcal{E}, \vec{R})$, where components are given by

[in the following we omit (...), so $\mathcal{G}_{\gamma\eta}$ means $\mathcal{G}_{\gamma\eta}(\mathcal{E}, \vec{R})$]

$$G^{\uparrow\uparrow}_{\text{Te Te}} = \mathcal{G}_{11}/2, \quad G^{\uparrow\downarrow}_{\text{Te Te}} = \mathcal{G}_{12}/2, \quad \text{(A1a)}$$

$$G^{\downarrow\uparrow}_{\text{Te Te}} = \mathcal{G}_{21}/2, \quad G^{\downarrow\downarrow}_{\text{Te Te}} = \mathcal{G}_{22}/2, \quad \text{(A1b)}$$

$$G^{\uparrow\uparrow}_{\text{Te Sn}} = \mathcal{G}_{12}/2, \quad G^{\uparrow\downarrow}_{\text{Te Sn}} = \mathcal{G}_{11}/2, \quad \text{(A1c)}$$

$$G^{\downarrow\uparrow}_{\text{Te Sn}} = \mathcal{G}_{22}/2, \quad G^{\downarrow\downarrow}_{\text{Te Sn}} = \mathcal{G}_{21}/2, \quad \text{(A1d)}$$

$$G^{\uparrow\uparrow}_{\text{Sn Te}} = \mathcal{G}_{21}/2, \quad G^{\uparrow\downarrow}_{\text{Sn Te}} = \mathcal{G}_{22}/2, \quad \text{(A1e)}$$

$$G^{\downarrow\uparrow}_{\text{Sn Te}} = \mathcal{G}_{11}/2, \quad G^{\downarrow\downarrow}_{\text{Sn Te}} = \mathcal{G}_{12}/2, \quad \text{(A1f)}$$

$$G^{\uparrow\uparrow}_{\text{Sn Sn}} = \mathcal{G}_{22}/2, \quad G^{\uparrow\downarrow}_{\text{Sn Sn}} = \mathcal{G}_{21}/2, \quad \text{(A1g)}$$

$$G^{\downarrow\uparrow}_{\text{Sn Sn}} = \mathcal{G}_{12}/2, \quad G^{\downarrow\downarrow}_{\text{Sn Sn}} = \mathcal{G}_{11}/2. \quad \text{(A1h)}$$

APPENDIX B: COMPONENTS OF THE SPIN SUSCEPTIBILITY

The spin susceptibility is described by $\chi^{\alpha\beta}_{lj}(\vec{R}) = -\frac{2}{\pi} \operatorname{Im} \int^{\mu}_{-\infty} d\mathcal{E} \, \mathbb{F}^{\alpha\beta}_{lj}(\mathcal{E}, \vec{R})$ with the following expressions for the first configuration (impurities on the same sublattices):

$$\mathbb{F}^{\alpha\alpha}_{xx} = \frac{|f(\vec{R})|^2}{4} \left[2\mathcal{G}_{11}\mathcal{G}_{22} - \mathcal{G}^2_{12} - \mathcal{G}^2_{21} \right], \quad \text{(B1a)}$$

$$\mathbb{F}^{\alpha\alpha}_{yy} = \frac{|f(\vec{R})|^2}{4} \left[2\mathcal{G}_{11}\mathcal{G}_{22} + \mathcal{G}^2_{12} + \mathcal{G}^2_{21} \right], \quad \text{(B1b)}$$

$$\mathbb{F}^{\alpha\alpha}_{zz} = \frac{|f(\vec{R})|^2}{4} \left[2\mathcal{G}_{12}\mathcal{G}_{21} + \mathcal{G}^2_{11} + \mathcal{G}^2_{22} \right], \quad \text{(B1c)}$$

$$\mathbb{F}^{\alpha\alpha,\alpha_s}_{xy/yx} = i\alpha_s \frac{|f(\vec{R})|^2}{4} \left[\mathcal{G}^2_{21} - \mathcal{G}^2_{12} \right], \quad \text{(B1d)}$$

$$\mathbb{F}^{\alpha\alpha,\alpha_s}_{xz/zx} = \pm\alpha_s \frac{|f(\vec{R})|^2}{4} [\mathcal{G}_{11} + \mathcal{G}_{22}][\mathcal{G}_{21} - \mathcal{G}_{12}], \quad \text{(B1e)}$$

$$\mathbb{F}^{\alpha\alpha}_{yz/zy} = \mp i \frac{|f(\vec{R})|^2}{4} [\mathcal{G}_{11} + \mathcal{G}_{22}][\mathcal{G}_{12} + \mathcal{G}_{21}]. \quad \text{(B1f)}$$

For the second configuration (impurities on different sublattices), we achieve

$$\mathbb{F}^{\alpha\beta/\beta\alpha}_{xx} = \frac{|f(\vec{R})|^2}{4} \left[2\mathcal{G}_{11}\mathcal{G}_{22} - \mathcal{G}^2_{12} - \mathcal{G}^2_{21} \right], \quad \text{(B2a)}$$

$$\mathbb{F}^{\alpha\beta/\beta\alpha}_{yy} = \frac{|f(\vec{R})|^2}{4} \left[-2\mathcal{G}_{11}\mathcal{G}_{22} - \mathcal{G}^2_{12} - \mathcal{G}^2_{21} \right], \quad \text{(B2b)}$$

$$\mathbb{F}^{\alpha\beta/\beta\alpha}_{zz} = \frac{|f(\vec{R})|^2}{4} \left[-2\mathcal{G}_{12}\mathcal{G}_{21} - \mathcal{G}^2_{11} - \mathcal{G}^2_{22} \right], \quad \text{(B2c)}$$

$$\mathbb{F}^{\alpha\beta,\alpha_d}_{xy/yx} = \pm i\alpha_d \frac{|f(\vec{R})|^2}{4} \left[\mathcal{G}^2_{12} - \mathcal{G}^2_{21} \right], \quad \text{(B2d)}$$

$$\mathbb{F}^{\alpha\beta,\alpha_d}_{xz/zx} = \alpha_d \frac{|f(\vec{R})|^2}{4} [\mathcal{G}_{11} + \mathcal{G}_{22}][\mathcal{G}_{12} - \mathcal{G}_{21}], \quad \text{(B2e)}$$

$$\mathbb{F}^{\alpha\beta}_{yz/zy} = \pm i \frac{|f(\vec{R})|^2}{4} [\mathcal{G}_{11} + \mathcal{G}_{22}][\mathcal{G}_{12} + \mathcal{G}_{21}]. \quad \text{(B2f)}$$

APPENDIX C: BEATING OSCILLATION OF RKKY INTERACTION

Here, we aim at showing the beating type of oscillations from multiple Dirac cones on the SnTe(001) surface [see
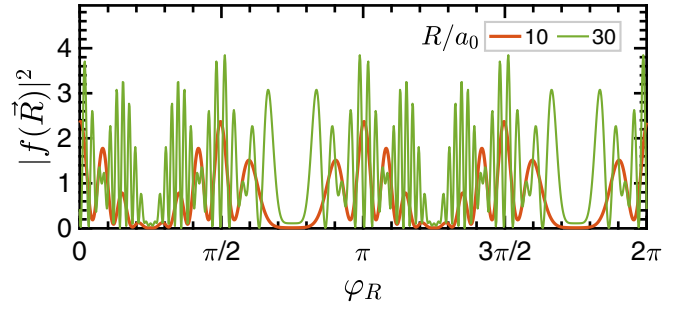

FIG. 6. Beating type of RKKY oscillations due to the multiple Dirac cones on the SnTe(001) surface, Eq. (15), for impurity separations $R/a_0 = 10$ and 30 as a function of the polar angle φ_R.

Eq. (15) for $|f(\vec{R})|^2$, as shown in Fig. 6]. The momenta contributed to this beating function are $X_{1/2} \pm \Lambda_{x/y}$ and $2\Lambda_{x/y}$ on the SBZ [53].

APPENDIX D: FLOQUET ENGINEERING OF MAGNETIC MOMENTS ALIGNMENT ON THE SnTe(001) SURFACE

An important motivation for Fig. 7 presented here originates from the spintronics community where the quest for
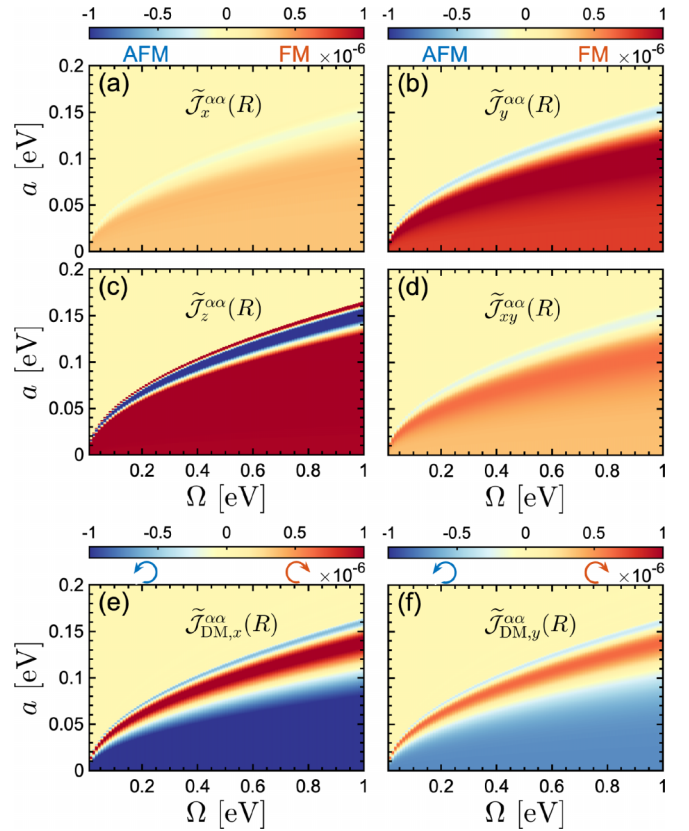

FIG. 7. Magnetic phase diagram of RKKY interactions on the driven-doped SnTe(001) surface at $R/a_0 = 50$ and $\varphi_R = \pi/3$. Depending on the interplay between light intensity a and frequency Ω, various FM/AFM and clockwise/counterclockwise characters can be seen for symmetric and asymmetric components, respectively. Also, $\tilde{\mathcal{J}}^{\alpha\alpha}_z(R) > \tilde{\mathcal{J}}^{\alpha\alpha}_{\text{DM},x}(R)$ holds true.
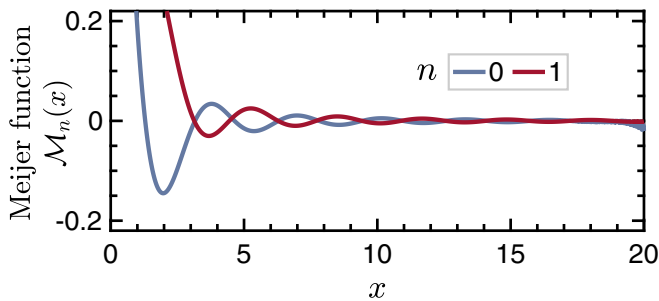
FIG. 8. Oscillatory Meijer functions, Eq. (E2), vs $x = \mu R/v_F$ for the undriven-doped SnTe(001) surface, resulting in oscillatory RKKY interactions in Fig. 3(b).

the control of magnetic phases is still active. Among the fundamental open questions is whether the magnetic moments alignment on the SnTe(001) surface with a nontrivial spin texture is adjustable through the interplay between the intensity and frequency of light. This is somehow important for the Floquet engineering of surfaces. As can be seen, phase diagrams for symmetric and asymmetric contributions

to the RKKY interaction highlight the characters of FM/AFM [for symmetric contributions in Figs. 7(a)–7(d)] as well as clockwise/counterclockwise [for asymmetric contributions in Figs. 7(e)–7(f)] in different controlled ways, characterized by red and blue colors. In a certain regime above the line $a \propto \sqrt{\Omega}$, the RKKY interaction vanishes. Getting away from the alignments, we have the relation $\widetilde{\mathcal{J}}_z^{\alpha\alpha}(R) > \widetilde{\mathcal{J}}_{\mathrm{DM},x}^{\alpha\alpha}(R)$ between the strongest symmetric and asymmetric RKKY components.

APPENDIX E: SOLUTION OF INTEGRALS IN EQ. (16) FOR UNDRIVEN-UNDOPED, UNDRIVEN-DOPED, AND DRIVEN-UNDOPED SnTe(001) SURFACES

In this part, we present the analytical expressions for the integrals in Eq. (16). For the pristine surface, we use the following relation for $n = \{0, 1\}$:

$$\mathrm{Im} \int_{o^+}^{\infty} i d\omega\, \omega^2 \mathbb{K}_n^2(\omega R/v_F) = +(2n+1)\frac{\pi^2 v_F^3}{32R^3}. \qquad (E1)$$

For the undriven-doped surface, the following relations are required to understand the short- and long-range responses:

$$\mathbb{K}_n(iu) = (-1)^{n+1}\frac{\pi}{2} e^{in\pi/2}[\mathbb{Y}_n(u) + i\mathbb{J}_n(u)], \qquad (E2a)$$

$$\mathrm{Im} \int_{o^+}^{\infty} i d\omega [\omega - i\mu]^2 \mathbb{K}_n^2([\omega - i\mu]R/v_F) = +(2n+1)\frac{\pi^2 v_F^3}{32R^3} - (-1)^n \frac{\pi^2 \mu^3}{4\sqrt{\pi}} \underbrace{\mathbb{G}_{2,4}^{2,1}\left(\begin{array}{c} -\frac{1}{2}, \frac{1}{2} \\ 0, n, -\frac{3}{2}, -n \end{array}\middle| \frac{\mu^2 R^2}{v_F^2}\right)}_{\mathcal{M}_n(\mu R/v_F)}, \qquad (E2b)$$

where $\mathcal{M}_n(x)$ is the special Meijer function [89,90], as shown in Fig. 8, which leads to oscillatory RKKY interactions in Fig. 3(b).

For the driven-undoped surface, we use the following mathematical identity [102]:

$$\int_{-\infty}^{0} x^{j-1} dx\, \mathbb{K}_n(ax)\mathbb{K}_m(ax) = \frac{2^{j-3}}{a^j \Gamma(j)} \Gamma([j+n+m]/2)\Gamma([j+n-m]/2)\Gamma([j-n+m]/2)\Gamma([j-n-m]/2), \qquad (E3)$$

where $\Gamma(\dots)$ is the Gamma function.

[1] M. Z. Hasan and C. L. Kane, Colloquium: Topological insulators, Rev. Mod. Phys. **82**, 3045 (2010).

[2] X.-L. Qi and S.-C. Zhang, Topological insulators and superconductors, Rev. Mod. Phys. **83**, 1057 (2011).

[3] H. Zhang, C.-X. Liu, X.-L. Qi, X. Dai, Z. Fang, and S.-C. Zhang, Topological insulators in Bi_2Se_3, Bi_2Te_3 and Sb_2Te_3 with a single dirac cone on the surface, Nat. Phys. **5**, 438 (2009).

[4] J. E. Moore and L. Balents, Topological invariants of time-reversal-invariant band structures, Phys. Rev. B **75**, 121306(R) (2007).

[5] R. Yu, W. Zhang, H.-J. Zhang, S.-C. Zhang, X. Dai, and Z. Fang, Quantized anomalous Hall effect in magnetic topological insulators, Science **329**, 61 (2010).

[6] C.-Z. Chang, J. Zhang, X. Feng, J. Shen, Z. Zhang, M. Guo, K. Li, Y. Ou, P. Wei, L.-L. Wang *et al.*, Experimental observation of the quantum anomalous Hall effect in a magnetic topological insulator, Science **340**, 167 (2013).

[7] X. Kou, S.-T. Guo, Y. Fan, L. Pan, M. Lang, Y. Jiang, Q. Shao, T. Nie, K. Murata, J. Tang *et al.*, Scale-Invariant Quantum Anomalous Hall Effect in Magnetic Topological Insulators beyond the Two-Dimensional Limit, Phys. Rev. Lett. **113**, 137201 (2014).

[8] J. G. Checkelsky, R. Yoshimi, A. Tsukazaki, K. S. Takahashi, Y. Kozuka, J. Falson, M. Kawasaki, and Y. Tokura, Trajectory of the anomalous Hall effect towards the quantized state in a ferromagnetic topological insulator, Nat. Phys. **10**, 731 (2014).

[9] H. Chi and J. S. Moodera, Progress and prospects in the quantum anomalous Hall effect, APL Mater. **10**, 090903 (2022).

[10] Z. Zhou, Y.-J. Chien, and C. Uher, Thin film dilute ferromagnetic semiconductors $Sb_{2-x}Cr_xTe_3$ with a curie temperature up to 190 K, Phys. Rev. B **74**, 224418 (2006).

[11] D. Zhang, A. Richardella, D. W. Rench, S.-Y. Xu, A. Kandala, T. C. Flanagan, H. Beidenkopf, A. L. Yeats, B. B. Buckley, P. V. Klimov, D. D. Awschalom, A. Yazdani, P. Schiffer, M. Z. Hasan, and N. Samarth, Interplay between ferromagnetism, surface states, and quantum corrections in a magnetically doped topological insulator, Phys. Rev. B **86**, 205127 (2012).

[12] Y. S. Hor, P. Roushan, H. Beidenkopf, J. Seo, D. Qu, J. G. Checkelsky, L. A. Wray, D. Hsieh, Y. Xia, S.-Y. Xu *et al.*,

Development of ferromagnetism in the doped topological insulator Bi$_{2-x}$Mn$_x$Te$_3$, Phys. Rev. B **81**, 195203 (2010).

[13] C.-Z. Chang, W. Zhao, D. Y. Kim, H. Zhang, B. A. Assaf, D. Heiman, S.-C. Zhang, C. Liu, M. H. W. Chan, and J. S. Moodera, High-precision realization of robust quantum anomalous Hall state in a hard ferromagnetic topological insulator, Nat. Mater. **14**, 473 (2015).

[14] T. R. F. Peixoto, H. Bentmann, S. Schreyeck, M. Winnerlein, C. Seibel, H. Maaß, M. Al-Baidhani, K. Treiber, S. Schatz, S. Grauer, C. Gould, K. Brunner, A. Ernst, L. W. Molenkamp, and F. Reinert, Impurity states in the magnetic topological insulator V : (Bi, Sb)$_2$te$_3$, Phys. Rev. B **94**, 195140 (2016).

[15] T. R. F. Peixoto, H. Bentmann, P. Rüßmann, A.-V. Tcakaev, M. Winnerlein, S. Schreyeck, S. Schatz, R. C. Vidal, F. Stier, V. Zabolotnyy *et al.*, Non-local effect of impurity states on the exchange coupling mechanism in magnetic topological insulators, npj Quantum Mater. **5**, 87 (2020).

[16] J. Wang, B. Lian, and S.-C. Zhang, Electrically Tunable Magnetism in Magnetic Topological Insulators, Phys. Rev. Lett. **115**, 036805 (2015).

[17] Q. Liu, C.-X. Liu, C. Xu, X.-L. Qi, and S.-C. Zhang, Magnetic Impurities on the Surface of a Topological Insulator, Phys. Rev. Lett. **102**, 156603 (2009).

[18] T. Kasuya, A Theory of Metallic Ferro- and Antiferromagnetism on Zener's Model, Prog. Theor. Phys. **16**, 45 (1956); K. Yosida, Magnetic properties of Cu-Mn alloys, Phys. Rev. **106**, 893 (1957); M. A. Ruderman and C. Kittel, Indirect exchange coupling of nuclear magnetic moments by conduction electrons, *ibid.* **96**, 99 (1954).

[19] F. Parhizgar, H. Rostami, and R. Asgari, Indirect exchange interaction between magnetic adatoms in monolayer MoS$_2$, Phys. Rev. B **87**, 125401 (2013).

[20] J. Klinovaja and D. Loss, RKKY interaction in carbon nanotubes and graphene nanoribbons, Phys. Rev. B **87**, 045422 (2013).

[21] V. E. Dmitrienko, E. N. Ovchinnikova, J. Kokubun, and K. Ishida, Dzyaloshinskii-Moriya interaction: How to measure its sign in weak ferromagnets? JETP Lett. **92**, 383 (2010).

[22] D. D. Awschalom and M. E. Flatté, Challenges for semiconductor spintronics, Nat. Phys. **3**, 153 (2007).

[23] R. Hanson, L. P. Kouwenhoven, J. R. Petta, S. Tarucha, and L. M. K. Vandersypen, Spins in few-electron quantum dots, Rev. Mod. Phys. **79**, 1217 (2007).

[24] I. Garate and M. Franz, Magnetoelectric response of the time-reversal invariant helical metal, Phys. Rev. B **81**, 172408 (2010).

[25] D. A. Abanin and D. A. Pesin, Ordering of Magnetic Impurities and Tunable Electronic Properties of Topological Insulators, Phys. Rev. Lett. **106**, 136802 (2011).

[26] D. K. Efimkin and V. Galitski, Self-consistent theory of ferromagnetism on the surface of a topological insulator, Phys. Rev. B **89**, 115431 (2014).

[27] J. Gao, W. Chen, X. C. Xie, and F.-c. Zhang, In-plane noncollinear exchange coupling mediated by helical edge states in quantum spin Hall systems, Phys. Rev. B **80**, 241302(R) (2009).

[28] P. D. Kurilovich, V. D. Kurilovich, and I. S. Burmistrov, Indirect exchange interaction between magnetic impurities in the two-dimensional topological insulator based on cdte/hgte/cdte quantum wells, Phys. Rev. B **94**, 155408 (2016).

[29] O. M. Yevtushenko and V. I. Yudson, Kondo Impurities Coupled to a Helical Luttinger Liquid: RKKY-Kondo Physics Revisited, Phys. Rev. Lett. **120**, 147201 (2018).

[30] A. A. Zyuzin and D. Loss, RKKY interaction on surfaces of topological insulators with superconducting proximity effect, Phys. Rev. B **90**, 125443 (2014).

[31] Emmanuel V. C. Lopes, E. Vernek, and T. M. Schmidt, RKKY interactions mediated by topological states in transition metal doped bismuthene, arXiv:2210.14658.

[32] M. V. Hosseini, Z. Karimi, and J. Davoodi, Indirect exchange interaction between magnetic impurities in one-dimensional gapped helical states, J. Phys.: Condens. Matter **33**, 085801 (2020).

[33] L. Fu, Topological Crystalline Insulators, Phys. Rev. Lett. **106**, 106802 (2011).

[34] T. H. Hsieh, H. Lin, J. Liu, W. Duan, A. Bansil, and L. Fu, Topological crystalline insulators in the snte material class, Nat. Commun. **3**, 982 (2012).

[35] Y. Tanaka, Z. Ren, T. Sato, K. Nakayama, S. Souma, T. Takahashi, K. Segawa, and Y. Ando, Experimental realization of a topological crystalline insulator in snte, Nat. Phys. **8**, 800 (2012).

[36] P. Dziawa, B. J. Kowalski, K. Dybko, R. Buczko, A. Szczerbakow, M. Szot, E. Łusakowska, T. Balasubramanian, B. M. Wojek, M. H. Berntsen *et al.*, Topological crystalline insulator states in Pb$_{1-x}$Sn$_x$Se, Nat. Mater. **11**, 1023 (2012).

[37] S.-Y. Xu, C. Liu, N. Alidoust, M. Neupane, D. Qian, I. Belopolski, J. D. Denlinger, Y. J. Wang, H. Lin, L. A. Wray *et al.*, Observation of a topological crystalline insulator phase and topological phase transition in Pb$_{1-x}$Sn$_x$Te, Nat. Commun. **3**, 1192 (2012).

[38] A. Kundu, H. A. Fertig, and B. Seradjeh, Floquet-Engineered Valleytronics in Dirac Systems, Phys. Rev. Lett. **116**, 016802 (2016).

[39] Y. J. Wang, W.-F. Tsai, H. Lin, S.-Y. Xu, M. Neupane, M. Z. Hasan, and A. Bansil, Nontrivial spin texture of the coaxial dirac cones on the surface of topological crystalline insulator snte, Phys. Rev. B **87**, 235317 (2013).

[40] M. Ezawa, Valleytronics on the surface of a topological crystalline insulator: Elliptic dichroism and valley-selective optical pumping, Phys. Rev. B **89**, 195413 (2014).

[41] T. Oka and H. Aoki, Photovoltaic Hall effect in graphene, Phys. Rev. B **79**, 081406(R) (2009).

[42] T. Oka and S. Kitamura, Floquet engineering of quantum materials, Annu. Rev. Condens. Matter Phys. **10**, 387 (2019).

[43] T. Kitagawa, T. Oka, A. Brataas, L. Fu, and E. Demler, Transport properties of nonequilibrium systems under the application of light: Photoinduced quantum Hall insulators without landau levels, Phys. Rev. B **84**, 235108 (2011).

[44] G. Platero and R. Aguado, Photon-assisted transport in semiconductor nanostructures, Phys. Rep. **395**, 1 (2004).

[45] M. M. Asmar and W.-K. Tse, Floquet control of indirect exchange interaction in periodically driven two-dimensional electron systems, New J. Phys. **23**, 123031 (2021).

[46] M. Ke and W.-K. Tse, Impurity states and indirect exchange interaction in irradiated graphene, Phys. Rev. B **106**, 075424 (2022).

[47] K. Nasu, *Photoinduced Phase Transitions* (World Scientific, Singapore, 2004).

[48] Z. Yan and Z. Wang, Tunable Weyl Points in Periodically Driven Nodal Line Semimetals, Phys. Rev. Lett. **117**, 087402 (2016).

[49] A. Narayan, Tunable point nodes from line-node semimetals via application of light, Phys. Rev. B **94**, 041409(R) (2016).

[50] M. Ezawa, hotoinduced topological phase transition from a crossing-line nodal semimetal to a multiple-Weyl semimetal, Phys. Rev. B **96**, 041205(R) (2017).

[51] A. Kundu and B. Seradjeh, Transport Signatures of Floquet Majorana Fermions in Driven Topological Superconductors, Phys. Rev. Lett. **111**, 136402 (2013).

[52] Z. Yang, Q. Yang, J. Hu, and D. E. Liu, Dissipative Floquet Majorana Modes in Proximity-Induced Topological Superconductors, Phys. Rev. Lett. **126**, 086801 (2021).

[53] M. Yarmohammadi and H. Cheraghchi, Effective low-energy RKKY interaction in doped topological crystalline insulators, Phys. Rev. B **102**, 075411 (2020).

[54] H. Cheraghchi and M. Yarmohammadi, Anisotropic ferroelectric distortion effects on the RKKY interaction in topological crystalline insulators, Sci. Rep. **11**, 5273 (2021).

[55] A. Fert, V. Cros, and J. Sampaio, Skyrmions on the track, Nat. Nanotechnol. **8**, 152 (2013).

[56] C. Liu, Y. Zang, W. Ruan, Y. Gong, K. He, X. Ma, Q.-K. Xue, and Y. Wang, Dimensional Crossover-Induced Topological Hall Effect in a Magnetic Topological Insulator, Phys. Rev. Lett. **119**, 176809 (2017).

[57] R. Wakatsuki, M. Ezawa, and N. Nagaosa, Domain wall of a ferromagnet on a three-dimensional topological insulator, Sci. Rep. **5**, 13638 (2015).

[58] J. Liu, W. Duan, and L. Fu, Two types of surface states in topological crystalline insulators, Phys. Rev. B **88**, 241303(R) (2013).

[59] M. Serbyn and L. Fu, Symmetry breaking and landau quantization in topological crystalline insulators, Phys. Rev. B **90**, 035402 (2014).

[60] Y. Okada, M. Serbyn, H. Lin, D. Walkup, W. Zhou, C. Dhital, M. Neupane, S. Xu, Y. J. Wang, R. Sankar *et al.*, Observation of dirac node formation and mass acquisition in a topological crystalline insulator, Science **341**, 1496 (2013).

[61] G. C. Paul, SK F. Islam, and A. Saha, Fingerprints of tilted dirac cones on the RKKY exchange interaction in 8-pmmn borophene, Phys. Rev. B **99**, 155418 (2019).

[62] M. Grifoni and P. Hänggi, Driven quantum tunneling, Phys. Rep. **304**, 229 (1998).

[63] J. H. Shirley, Solution of the Schrödinger equation with a hamiltonian periodic in time, Phys. Rev. **138**, B979 (1965).

[64] M. Busl, G. Platero, and A.-P. Jauho, Dynamical polarizability of graphene irradiated by circularly polarized ac electric fields, Phys. Rev. B **85**, 155449 (2012).

[65] N. Tsuji, T. Oka, and H. Aoki, Correlated electron systems periodically driven out of equilibrium: Floquet + DMFT formalism, Phys. Rev. B **78**, 235124 (2008).

[66] M. Ke, M. M. Asmar, and W.-K. Tse, Nonequilibrium RKKY interaction in irradiated graphene, Phys. Rev. Res. **2**, 033228 (2020).

[67] T. Kitagawa, E. Berg, M. Rudner, and E. Demler, Topological characterization of periodically driven quantum systems, Phys. Rev. B **82**, 235114 (2010).

[68] M. Ezawa, Photoinduced Topological Phase Transition and a Single Dirac-Cone State in Silicene, Phys. Rev. Lett. **110**, 026603 (2013).

[69] H. L. Calvo, H. M. Pastawski, S. Roche, and L. E. F. F. Torres, Tuning laser-induced band gaps in graphene, Appl. Phys. Lett. **98**, 232103 (2011).

[70] Y. Zhou and M. W. Wu, Optical response of graphene under intense terahertz fields, Phys. Rev. B **83**, 245436 (2011).

[71] E. Kogan, RKKY interaction in gapped or doped graphene, Graphene **02**, 8 (2013).

[72] M. Sherafati and S. Satpathy, RKKY interaction in graphene from the lattice Green's function, Phys. Rev. B **83**, 165425 (2011).

[73] M. Sherafati and S. Satpathy, Analytical expression for the RKKY interaction in doped graphene, Phys. Rev. B **84**, 125416 (2011).

[74] M. S. Rudner and N. H. Lindner, Band structure engineering and non-equilibrium dynamics in Floquet topological insulators, Nat. Rev. Phys. **2**, 229 (2020).

[75] H. Imamura, P. Bruno, and Y. Utsumi, Twisted exchange interaction between localized spins embedded in a one- or two-dimensional electron gas with Rashba spin-orbit coupling, Phys. Rev. B **69**, 121303(R) (2004).

[76] J.-J. Zhu, D.-X. Yao, S.-C. Zhang, and K. Chang, Electrically Controllable Surface Magnetism on the Surface of Topological Insulators, Phys. Rev. Lett. **106**, 097201 (2011).

[77] M. Shiranzaei, H. Cheraghchi, and F. Parhizgar, Effect of the Rashba splitting on the RKKY interaction in topological-insulator thin films, Phys. Rev. B **96**, 024413 (2017).

[78] R. Cheng, S. Okamoto, and D. Xiao, Spin Nernst Effect of Magnons in Collinear Antiferromagnets, Phys. Rev. Lett. **117**, 217202 (2016).

[79] S. K. Kim, H. Ochoa, R. Zarzuela, and Y. Tserkovnyak, Realization of the Haldane-Kane-Mele Model in a System of Localized Spins, Phys. Rev. Lett. **117**, 227201 (2016).

[80] L. Chen, J.-H. Chung, B. Gao, T. Chen, M. B. Stone, A. I. Kolesnikov, Q. Huang, and P. Dai, Topological Spin Excitations in Honeycomb Ferromagnet cri₃, Phys. Rev. X **8**, 041028 (2018).

[81] J. Sampaio, V. Cros, S. Rohart, A. Thiaville, and A. Fert, Nucleation, stability and current-induced motion of isolated magnetic skyrmions in nanostructures, Nat. Nanotechnol. **8**, 839 (2013).

[82] M. M. Asmar and W.-K. Tse, Interlayer RKKY coupling in bulk rashba semiconductors under topological phase transition, Phys. Rev. B **100**, 014410 (2019).

[83] V. K. Dugaev, V. I. Litvinov, and J. Barnas, Exchange interaction of magnetic impurities in graphene, Phys. Rev. B **74**, 224438 (2006).

[84] S. Saremi, RKKY in half-filled bipartite lattices: Graphene as an example, Phys. Rev. B **76**, 184430 (2007).

[85] A. M. Black-Schaffer, RKKY coupling in graphene, Phys. Rev. B **81**, 205416 (2010).

[86] J. Chen, H. J. Qin, F. Yang, J. Liu, T. Guan, F. M. Qu, G. H. Zhang, J. R. Shi, X. C. Xie, C. L. Yang *et al.*, Gate-Voltage Control of Chemical Potential and Weak Antilocalization in bi₂se₃, Phys. Rev. Lett. **105**, 176602 (2010).

[87] A. L. Yeats, P. J. Mintun, Y. Pan, A. Richardella, B. B. Buckley, N. Samarth, and D. D. Awschalom, Local optical

control of ferromagnetism and chemical potential in a topological insulator, Proc. Natl. Acad. Sci. USA **114**, 10379 (2017).

[88] R. W. Schoenlein, S. Chattopadhyay, H. H. W. Chong, T. E. Glover, P. A. Heimann, C. V. Shank, A. A. Zholents, and M. S. Zolotorev, Generation of femtosecond pulses of synchrotron radiation, Science **287**, 2237 (2000).

[89] Y. L. Luke, *The Special Functions and Their Approximations* (Elsevier, Amsterdam, 1969).

[90] J. L. Fields, The asymptotic expansion of the Meijer G-function, Math. Comput. **26**, 757 (1972).

[91] Y. H. Wang, H. Steinberg, P. Jarillo-Herrero, and N. Gedik, Observation of Floquet-Bloch states on the surface of a topological insulator, Science **342**, 453 (2013).

[92] M. Nuske, L. Broers, B. Schulte, G. Jotzu, S. A. Sato, A. Cavalleri, A. Rubio, J. W. McIver, and L. Mathey, Floquet dynamics in light-driven solids, Phys. Rev. Res. **2**, 043408 (2020).

[93] J. W. McIver, B. Schulte, F.-U. Stein, T. Matsuyama, G. Jotzu, G. Meier, and A. Cavalleri, Light-induced anomalous Hall effect in graphene, Nat. Phys. **16**, 38 (2020).

[94] A. T. Hindmarch and B. J. Hickey, Direct Experimental Evidence for the Ruderman-Kittel-Kasuya-Yosida Interaction in Rare-Earth Metals, Phys. Rev. Lett. **91**, 116601 (2003).

[95] A. A. Khajetoorians, J. Wiebe, B. Chilian, S. Lounis, S. Blügel, and R. Wiesendanger, Atom-by-atom engineering and magnetometry of tailored nanomagnets, Nat. Phys. **8**, 497 (2012).

[96] L. Zhou, J. Wiebe, S. Lounis, E. Vedmedenko, F. Meier, S. Blügel, P. H. Dederichs, and R. Wiesendanger, Strength and directionality of surface Ruderman-Kittel-Kasuya-Yosida interaction mapped on the atomic scale, Nat. Phys. **6**, 187 (2010).

[97] M. Yarmohammadi, C. Meyer, B. Fauseweh, B. Normand, and G. S. Uhrig, Dynamical properties of a driven dissipative dimerized $s = \frac{1}{2}$ chain, Phys. Rev. B **103**, 045132 (2021).

[98] J. Hausinger and M. Grifoni, Dissipative two-level system under strong ac driving: A combination of Floquet and Van Vleck perturbation theory, Phys. Rev. A **81**, 022117 (2010).

[99] S. Park, H. Min, E. H. Hwang, and S. Das Sarma, Diluted magnetic Dirac-Weyl materials: Susceptibility and ferromagnetism in three-dimensional chiral gapless semimetals, Phys. Rev. B **98**, 064425 (2018).

[100] H. Min, E. H. Hwang, and S. Das Sarma, Ferromagnetism in chiral multilayer two-dimensional semimetals, Phys. Rev. B **95**, 155414 (2017).

[101] M. Shiranzaei, J. Fransson, H. Cheraghchi, and F. Parhizgar, Nonlinear spin susceptibility in topological insulators, Phys. Rev. B **97**, 180402(R) (2018).

[102] A. P. Prudnikov, I. U. A. Brychkov, I. U. A. Brychkov, and O. I. Marichev, *Integrals and Series: Special functions*, Integrals and Series (Gordon and Breach, New York, 1986).